# EBSD and Nanoindentation-Correlated Study of Delamination Fracture in Al-Li Alloy 2090

W. Tayon[1*]; R. Crooks[2]; M. Domack[3]; J. Wagner[3]; A. A. Elmustafa[1]

[1]*Department of Mechanical Engineering, The Applied Research Center, Old Dominion University, Norfolk, VA 23529*
[2]*National Institute of Aerospace, Hampton, VA 23666*
[3]*NASA Langley Research Center, Hampton, VA 23681*

**Abstract:**

Al-Li alloys offer attractive combinations of high strength and low density. However, a tendency for delamination fracture has limited their use. A better understanding of the delamination mechanisms may identify methods to control delaminations through processing modifications. A combination of new techniques has been used to evaluate delamination fracture in Al-Li alloys. Both high quality electron backscattered diffraction (EBSD) information and valid nanoindentation measurements were obtained from fractured test specimens. Correlations were drawn between nano-scale hardness variations and local texture along delaminating boundaries. Intriguing findings were observed for delamination fracture through the combined analysis of grain orientation, Taylor factor, and kernel average misorientation.

*Keywords:* delamination; Al-Li alloy; nano hardness; EBSD; kernel average misorientation; KAM; Taylor factor; twin-related variants

* Corresponding author:  Tel. 1 + 757-269-6067
E-mail address: wtayo001@odu.edu (W. Tayon)

## 1. Introduction

Al-Li alloys are of interest for use in aerospace structures due to the desirable combination of high strength and low density of this class of alloys. In the early 1990's, the weight of the ~ 60,000 lb Space Shuttle External Tank (ET) was reduced by ~ 7500 lb by redesigning the tank and replacing aluminum alloy 2219 with Al-Li 2195. The intertank structure of the ET is fabricated from sheet gage Al-Li alloy 2090. In general, however, Al-Li alloys have found limited structural application due, in part, to the propensity for Al alloys with Li content greater than approximately 1.0% to exhibit a delamination fracture mode [1]. Delamination fracture is characterized by secondary failure along elongated grain boundaries perpendicular to the primary advancing crack (Fig. 1). Aerospace designers have found it difficult to account for and model this type of fracture, thus, limiting the use of some of the lower density Al-Li alloys.
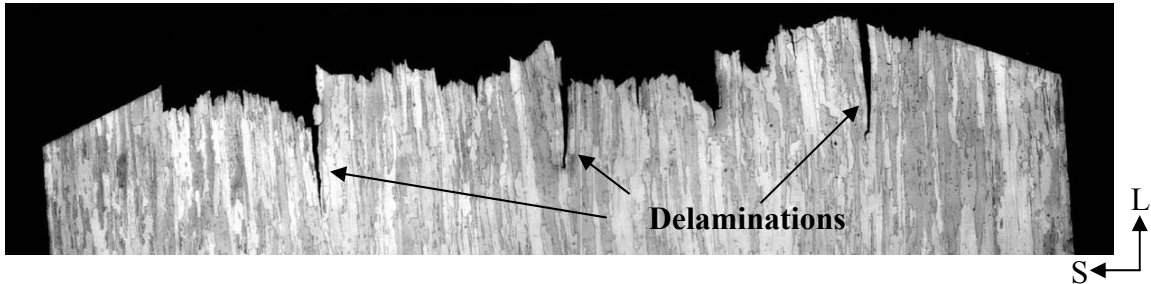


**Fig. 1    Metallurgical section of L-S plane exhibiting delamination fracture.**

The current study investigated delamination behavior in a 2090-T81 plate alloy using electron backscattered diffraction (EBSD) analyses to define grain orientations and grain boundary types and nano indentation studies to measure grain-to-grain variations in nano hardness in grains adjacent to delaminations. The goal of the study was to develop a better understanding of the delamination fracture mechanisms in Al-Li alloys, which may enable plate processing modifications to reduce or eliminate delaminations. Prior studies [2] have shown that not all boundaries are susceptible to delamination fracture, and the distribution of delamination

cracks varies from sample to sample. Previous EBSD analyses of 2090 [2] showed that the boundaries which delaminate have greater than 30º misorientation. Furthermore, the amount of substructure changed abruptly at the delaminating boundaries. While one grain showed a large amount of stored strain energy, the adjacent grain appeared to be recrystallized. Preliminary nanoindentation studies of the grains adjacent to delaminations revealed an increase in nanohardness of approximately 20% across a single delamination, suggesting that nanoindentation may be a useful method to quantify retained deformation within grains stored during cold working.

## 2. Materials

The material evaluated during this study was commercially produced Al-Li alloy 2090-T81 plate, 19 mm thick. The nominal composition by weight percent was 2.85 Cu, 2.30 Li, 0.10 Zr, 0.07 Fe, balance Al. The typical microstructure at the mid-plane of the plate, shown in Fig. 2, exhibits a pancake grain morphology, elongated in the rolling direction, with aspect ratio of approximately 10:1 (L:S).
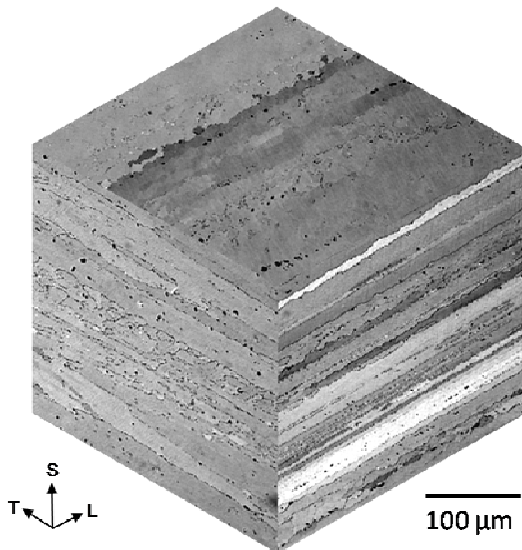


**Fig. 2    Tri-planar microstructure of 19 mm thick plate of 2090-T81.**

**3. Experimental Procedures**

3.1 Polishing

Compact-tension, C(T), fracture toughness specimens were sectioned after failure in the longitudinal-short transverse (LS) plane with a low speed saw. After sectioning, samples were mounted with cyanoacrylate adhesive on 30 mm diameter aluminum cylinders, which are the standard size mounts for the nano indenter. Samples were mechanically polished with a precision polishing apparatus to produce a flat, relatively-strain-free surface. Electropolishing methods were used in prior experimentation, but resulted in attack at grain boundaries and poor surface flatness. Flatness was found to be paramount for both EBSD and nanoindentation studies.

Mechanical polishing was performed with an automated polishing system. The depth of material removed was monitored with a micrometer dial gauge attached to the polishing head. The polishing system allowed application of load in increments of 100 grams, over a range of 0 to 600 grams. Prior to polishing, the platen and polishing head were aligned parallel to a tolerance of 3 μm or less.

The polishing procedure included: 600 grit SiC paper for 3 minutes at 125 rpm and 600 gram load, 1200 grit SiC paper for 6 minutes at 100 rpm and 400 gram load, 3 μm diamond paste for 8 minutes at 75 rpm and 300 gram load, and 1 μm diamond paste for 12 minutes at 75 rpm and 200 gram load. An alcohol-based lubricant was used in each step listed above. For the final polish, a 0.05 μm colloidal silica suspension was used for 1 hour at 50 rpm and 100 gram load. Medium-nap cloth pads were used for the diamond and final polishing stages. Samples were ultrasonically cleaned in ethanol after each abrasive step. After the final polish, samples were

rinsed with a neutral pH soap and tap water. This technique produced a flat, relatively-stain-free surface, with no apparent grain boundary damage.

3.2 Nanoindentation

Scanned regions near delamination cracks were investigated for potential hardness variations between adjacent grains along the fracture path. A nanoindenter with continuous stiffness measurement (CSM) capabilities was used to measure hardness. The CSM device allows for hardness data to be obtained as a continuous function of indentation depth. Indents were made with a three-sided Berkovich diamond indenter tip. The nanoindenter was calibrated using fused silica prior to testing. Hardness measurements were obtained from the sampled regions based on the Oliver and Pharr Method [3]. Indentation was conducted at several locations along delaminations, as shown in Fig. 3, to include the following: origination (opening) region, delamination termination (tip) region, and an unfractured region 800 µm from the tip. The delamination opening region sampled was generally within 100 µm from the intersection of the delamination with the primary crack. At each location, nano indents were placed in 5 x 5 arrays on each side of delamination fractures within the grains immediately above and below the fracture path. Each indent in the arrays was driven to a depth of 250 nm and separated by 10 µm in each direction.
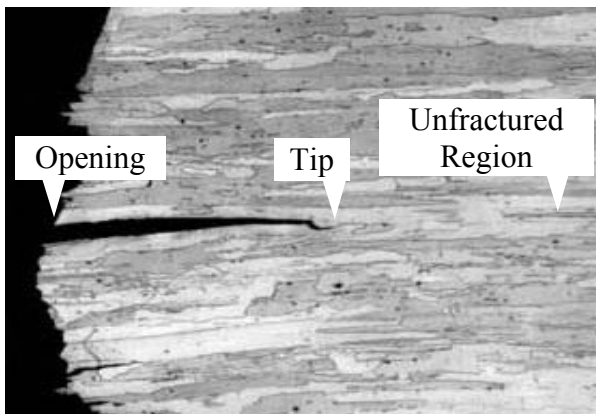


**Fig. 3    Delamination regions evaluated.**

3.3 Electron Backscattered Diffraction (EBSD)

Polished samples were analyzed in a scanning electron microscope (SEM) with a $LaB_6$ filament. A commercially-available diffraction camera with an EBSD pattern detection system was interfaced with data collection software. Samples were aligned with the rolling direction parallel to the x-axis and the transverse direction parallel to the y-axis. Samples were tilted to 70º and examined at an accelerating voltage of 20 kV. A software tilt correction was applied in order to account for the 70º tilt in the data collection. On average, the fraction of indexed patterns ("hit rate") was ninety percent or better for samples prepared by the aforementioned polishing protocol. A typical scanned region covered an area of roughly 400 x 600 points at 0.3 μm spatial resolution (step size). Scanned regions (opening, tip, unfractured region) corresponded to the same locations along delaminations that were evaluated with nano indentation.

A separate EBSD study was conducted to evaluate the through-thickness variation of texture components in 2090 from t/4 to t/2. This study sought to address the frequency of boundary types (or grain orientation pairs) similar to those found to delaminate.

3.4 Grain Orientation and Texture Analyses

The EBSD data sets were analyzed to yield grain boundary misorientation, kernel average misorientation, identification of grains by proximity to characteristic orientations (or texture components), and grain boundary orientation distribution functions. Detailed, color-coded maps, images and charts were produced where applicable. Orientation distribution functions (ODFs) and pole figures were calculated by harmonic series expansion. Sample orientation was verified by analyzing (100), (110), and (111) pole figures generated from the calculated ODFs. Kernel average misorientation (KAM) was calculated using the average

misorientation of a given pixel with its nearest neighbors within a defined distance (approximately 1 μm for this study), excluding misorientations greater than a pre-set tolerance value ($3^{o}$ for this study). The appearance of KAM may be interpreted as the amount of local lattice rotation. Taylor factors (TF) as a function of grain orientation were calculated based on stresses believed to contribute to delamination fracture.

## 4. Results and Discussion

4.1 Nanoindentation

Nanoindentation testing was used to evaluate grain-to-grain nanohardness variations in several regions along delamination fractures. Indentation data revealed that this Al-Li alloy exhibited a reverse indentation size effect (RISE). RISE is characterized by an increase in hardness with increasing indentation depth, which is the reverse of the indentation size effect (ISE) observed for other metallic materials in [4]. Fig. 4 illustrates typical hardness versus contact depth (depth of penetration) plots for indents at each region sampled. A single nanohardness value was determined for each indent based on an average of all the hardness data collected within the 100 to 200 nm range of contact depth, where the hardness was stabilized. From these results, average hardness values for grains directly above and below delaminations were calculated.
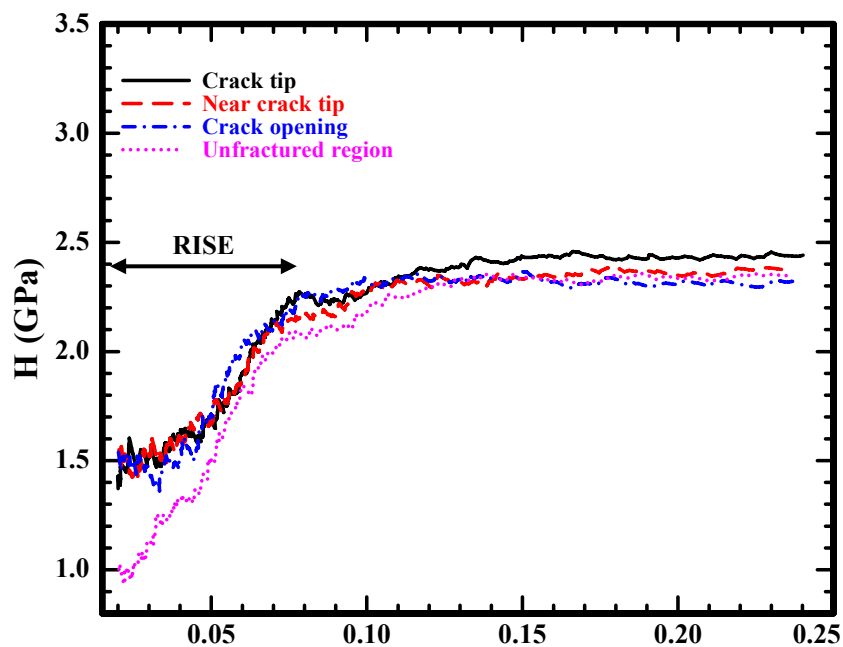
**Fig. 4** **Typical hardness vs depth plot for a single nanoindent at each region sampled. The range of data exhibiting the reverse indentation size effect (RISE) is noted by the arrow.**

The results from nanoindentation are shown in Table 1 for the opening, tip, and unfractured regions for three separate delaminations, representing a total of approximately 300 indents. Small differences in hardness were found in the surrounding grains adjacent to the fracture. The maximum percent difference in nanohardness between the grains above and below delamination fractures was roughly 7% for all regions sampled with an average value slightly above 3%. The largest differences were generally found in the opening region, ranging from 3 to 7% in the grains adjacent to the fracture. At regions around the delamination tip, hardness values were more uniform within a range of 0.5 to 3% for grains above and below the fracture. Small percent differences in nano hardness were also found along the same boundary in an unfractured region at a distance of 800 μm past the delamination tip. Large differences in hardness were not found in the grains adjacent to delaminations as previously indicated. Therefore, there does not appear to be a significant difference in the retained cold work within the grains.

**Table 1** Nanohardness Results at Opening, Tip, and Unfractured Regions for Three Delaminations

| Region | Delamination Number | Avg. Hardness Above Delamination, GPa (# indents) | Avg. Hardness Below Delamination, GPa (# indents) | Percent Difference, % |
|--------|--------------------|--------------------------------------------------|--------------------------------------------------|-----------------------|
| Opening | 1 | 2.25 (25) | 2.18 (24) | 3.20 |

| | 2 | 2.47 (16) | 2.33 (15) | 5.84 |
|---|---|---|---|---|
| | 3 | 2.80 (21) | 2.62 (15) | 6.79 |
| Delamination Tip | 1 | 2.39 (20) | 2.32 (21) | 3.56 |
| | 2 | 2.67 (13) | 2.65 (14) | 0.69 |
| | 3 | 2.68 (17) | 2.63 (14) | 1.95 |
| Unfractured Region (800 μm from tip) | 1 | 2.28 (19) | 2.25 (14) | 1.30 |
| | 2 | 2.48 (14) | 2.39 (20) | 3.64 |
| | 3 | 2.49 (13) | *** | *** |

***= Insufficient test data

## 4.2 Texture and Misorientation

Delamination cracks in aluminum-lithium alloys tend to occur along high angle grain boundaries with misorientations greater than 30º [2]. In this study, all delaminations occurred along grain boundaries with misorientations between 50º and 60º. The "Brass" grain orientation is commonly found in Al-Li-Zr alloys and Al-Cu-Zr alloys (e.g. Supral), and is prevalent in 2090 [2, 5-8]. The pole figures and ODFs in Fig. 5 show a well defined Brass texture. Face-centered cubic crystals have 24 equivalent orientations which can be obtained by rotation about crystal symmetry axes. Texture variants are related by 180º rotations about the orthotropic sample symmetry axes (RD, ND, TD) and share the same form of Miller indices. When these rotation axes do not coincide with the crystal symmetry axes, the variants are not crystallographically equivalent. Brass has two variants, equivalent to 180º rotation about the non-symmetric rolling direction axis, <2-1 1>. In this study, Bs1 is defined by the Euler angles (35, 45, 0) or Miller indices (011)[2-1 1] and Bs2 is defined by the Euler angles (55, 90, 45) or the Miller indices (110)[1-1 2].
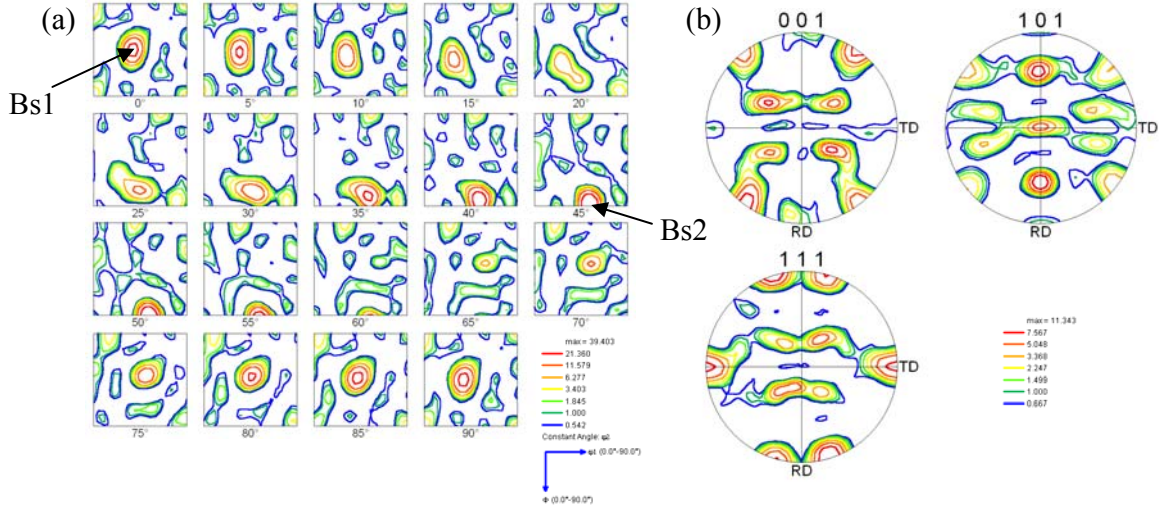
**Fig. 5    Texture results for 2090-T81 plate for the region from t/2 to t/4.    a) ODF showing ideal Brass orientation along β-fiber; b) Pole figures.**

Grain boundaries are typically characterized by misorientation, expressed as angle/axis pairs. Coincident site lattice (CSL) nomenclature, denoted as Σn (where n is the inverse of the fraction of lattice points common to both lattices), is used to categorize grain misorientations as low index (low Σ number) or high index (high Σ number). Ideal Brass variants show a low index misorientation, equivalent to a Σ3 (60°/<111>). The coherent twin misorientation in fcc polycrystalline materials is Σ3, with a {111} twin plane. All points on the {111} plane are common to both lattices. Since the grain boundary plane for the Brass grains in this study is close to {011}, the Bs1/Bs2 boundary is an "incoherent" twin. Incoherent boundaries are known to be high-energy boundaries; the boundary plane includes lattice sites which are not common to both crystals. A tendency for intergranular fracture along Brass texture variants was observed in the delaminations studied (Fig. 6). The fractured boundaries appeared qualitatively flatter and longer than other boundaries. The grains adjacent to the fracture were on the order of several millimeters in length and 50 to 200 μm in width with elongation-to-thickness aspect ratios near 10:1, as observed in [6].
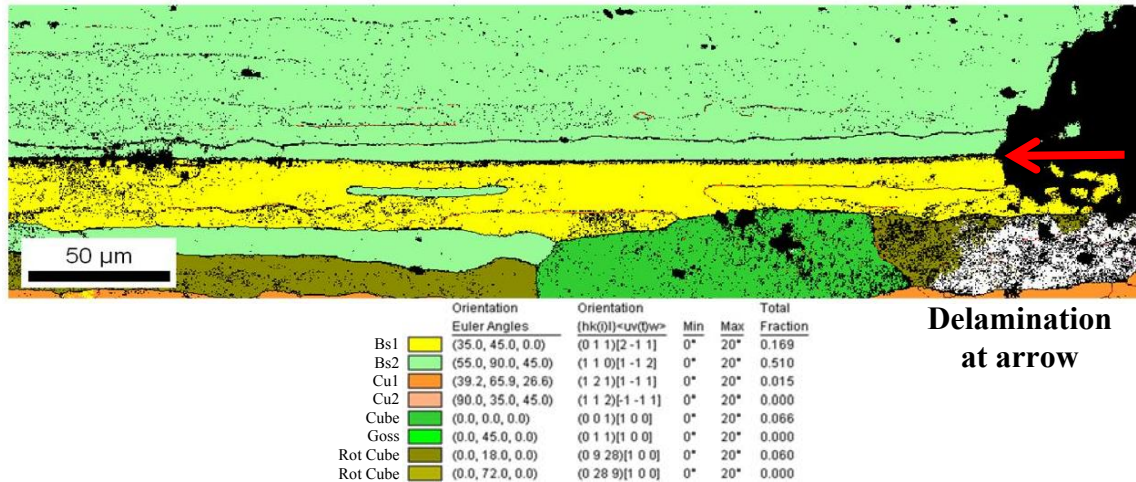
| | Orientation Euler Angles | Orientation (hk(i)l)<uv(t)w> | Min | Max | Total Fraction |
|---|---|---|---|---|---|
| Bs1 | (35.0, 45.0, 0.0) | (0 1 1)[2 -1 1] | 0° | 20° | 0.169 |
| Bs2 | (55.0, 90.0, 45.0) | (1 1 0)[1 -1 2] | 0° | 20° | 0.510 |
| Cu1 | (39.2, 65.9, 26.6) | (1 2 1)[1 -1 1] | 0° | 20° | 0.015 |
| Cu2 | (90.0, 35.0, 45.0) | (1 1 2)[-1 -1 1] | 0° | 20° | 0.000 |
| Cube | (0.0, 0.0, 0.0) | (0 0 1)[1 0 0] | 0° | 20° | 0.066 |
| Goss | (0.0, 45.0, 0.0) | (0 1 1)[1 0 0] | 0° | 20° | 0.000 |
| Rot Cube | (0.0, 18.0, 0.0) | (0 9 28)[1 0 0] | 0° | 20° | 0.060 |
| Rot Cube | (0.0, 72.0, 0.0) | (0 28 9)[1 0 0] | 0° | 20° | 0.000 |

**Delamination at arrow**

**Fig. 6    Typical texture components identified adjacent to delaminations.  The delamination in this image is noted by the arrow.**

In the through-thickness scans (beyond the delamination crack tips), numerous layers of Brass oriented grains were present within the sample as indicated in Fig. 7a. The EBSD software was used to color-code grain orientations to the nearest deformation texture component (within 20º of their respective ideal orientations), using the 12 most common (β-fiber) components and variants. Approximately 70% of the material from t/4 to t/2 was characterized as Bs1 or Bs2 grains; similar results were reported for Al-6Cu-0.4Zr [5, 6]. Two of the delaminations on the sample corresponded to locations within this large scanned area, as noted in Fig. 7a within the circled regions and marked by
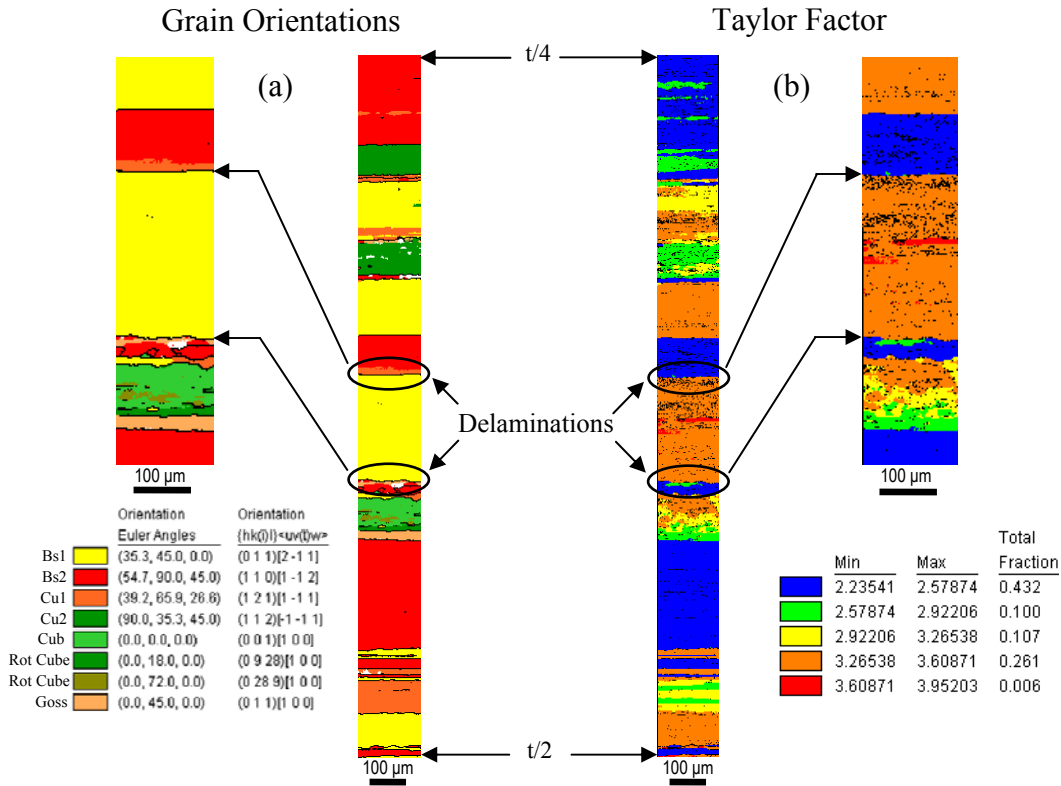
Grain Orientations      Taylor Factor

(a)     t/4     (b)

Delaminations

100 µm

| | Orientation Euler Angles | Orientation {hk(i)l}<uv(t)w> |
|---|---|---|
| Bs1 | (35.3, 45.0, 0.0) | (0 1 1)[2 -1 1] |
| Bs2 | (54.7, 90.0, 45.0) | (1 1 0)[1 -1 2] |
| Cu1 | (39.2, 65.9, 26.6) | (1 2 1)[1 -1 1] |
| Cu2 | (90.0, 35.3, 45.0) | (1 1 2)[-1 -1 1] |
| Cub | (0.0, 0.0, 0.0) | (0 0 1)[1 0 0] |
| Rot Cube | (0.0, 18.0, 0.0) | (0 9 28)[1 0 0] |
| Rot Cube | (0.0, 72.0, 0.0) | (0 28 9)[1 0 0] |
| Goss | (0.0, 45.0, 0.0) | (0 1 1)[1 0 0] |

| | Min | Max | Total Fraction |
|---|---|---|---|
| | 2.23541 | 2.57874 | 0.432 |
| | 2.57874 | 2.92206 | 0.100 |
| | 2.92206 | 3.26538 | 0.107 |
| | 3.26538 | 3.60871 | 0.261 |
| | 3.60871 | 3.95203 | 0.006 |

100 µm

t/2

100 µm     100 µm

**Fig. 7**    **Grain orientation and Taylor factor distributions for plate thickness from t/4 to t/2. Delaminations were found to occur at locations shown.   a) Distribution indicates predominance of Brass orientations, Bs1 and Bs2 and b) Taylor factor map indicating high and lowest TF associated with Brass orientations.**

arrows to the higher magnification view. Roughly 30% of the Bs1 grain boundaries in this region were bordered by a Bs2 grain. Therefore, the occurrence of twin-related Brass-variant grain boundaries was seen to be a common from t/4 to t/2, similar to results noted in [5].

4.3 Kernel Average Misorientation

Kernel average misorientation (KAM) shows local lattice distortion and may indicate stored-strain energy, localized deformation, and high dislocation density within a given region. Fig. 8 shows KAM for a typical delamination from the opening to tip regions with a magnified section shown of the tip. Sub-grain boundaries that fall within the pre-set misorientation limit of 3º appear as KAM and are particularly found in the grain above the fracture for the delamination

shown. These sub-grain boundaries should be disregarded since they share no relationship with the localized deformation analyzed by KAM. At the opening regions of delaminations, both sides contained significant KAM that was nearly equal in density and magnitude as seen in Fig. 8. Strong deformation in these regions was presumed to result from being within the plastic zone associated with the larger primary crack passing near the opening regions.
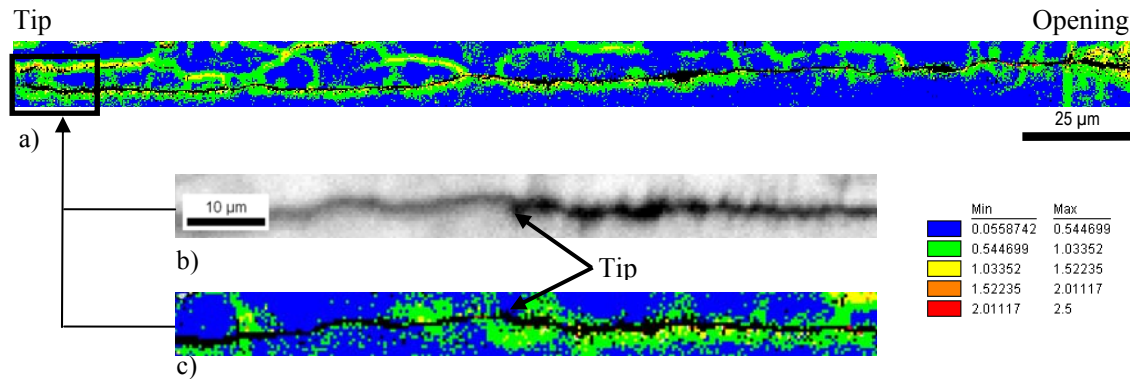


**Fig. 8** **KAM concentrations in grains bordering a delamination. (a) KAM distribution from opening to tip of a typical delamination, (b) Image quality map corresponding to the enlarged region highlighted in (a) near the tip region, and (c) KAM distribution for the same enlarged region.**

At regions further down the delamination, appreciable levels of KAM can be found on one side of the delamination boundary, but not the other. These long bands of KAM appear within approximately 5 μm of the fractured boundary. The KAM concentration appears to diminish near the tip of the delamination. The location of delamination tip was identified with an SEM and has been shown in Fig. 8, image (b). The much thinner, black line ahead of the tip represents the continuation of grain boundary which has not fractured. The higher levels of KAM on one side of the boundary are consistent with a lack of slip accommodation across the delaminating interface.

Significant differences in nanohardness are expected within a few microns of fractured boundaries, but only a few indents fell within that narrow region. The majority of the indents fell within grain interiors, approximately 5 to 10 μm away from the edge of the delamination. Future

13

research will address the connections between KAM and nano-scale properties. It is anticipated that larger differences in hardness will be found in these regions of increased KAM.

4.4 Taylor Factor

The Taylor theory for polycrystalline materials provides a means of predicting the anisotropy of deformation, based on the orientation distribution of a polycrystalline aggregate and the boundary conditions of individual grains. TSL OIM software was used in this study to produce maps of grain-specific Taylor factors (TF). Spatially-correlated orientation information from EBSD scans was analyzed in conjunction with a crystallographic description of the slip systems and assumptions about the loading environment (expressed as a stress tensor). Finite element simulations and mechanical test results performed at the University of Illinois indicated that the initiation and propagation of delamination cracks stemmed from a combination of normal and shear stresses at the grain boundary [9]. Generally, grain orientations with higher TFs exhibit a greater resistance to deformation [10].

When the TFs were computed for delaminating regions with the simultaneous consideration of normal stress and out-of-plane shear stress, $\sigma_{zz}$ and $\tau_{yz}$, there was a large disparity noticed between twin-related variants on either side of a fracture. The TFs for grains within the through-thickness scan from t/4 to t/2 are shown in Fig. 7b alongside grain orientations for the same region. The location of two delaminations noted previously within this region have been circled and noted with arrows. The location of the delaminations coincided with Bs1/Bs2 grain pairs which exhibited the largest difference in TF. Typically, one Brass variant had a lower TF around 2.6, while the other Brass variant on the opposing side of the fracture was typically near 3.5. These results show a correlation between delamination fracture

14

and TFs. Delaminations occur along boundaries with a distinct orientation difference; one which results in large TF differences between the grains.

## 4.5 TF and KAM correlation

A correlation was noted between the occurrence of KAM in grains bordering a delamination and TF, as illustrated in Fig. 9. Concentrations of KAM were observed along only one side of a delaminating interface. The grain exhibiting the narrow band of KAM was consistently the lower TF grain in the pair. Similar concentrations of KAM along low TF grain boundaries were observed in [10], where it was found that low TF grains sometimes behave as soft grains in the presence of high TF grains. The KAM and TF distributions observed in the current study support the hypothesis that a lack of slip accommodation across the interface, resulting in an excess of deformation damage on the (crystallographically) "softer" side, contributing to delamination fracture.
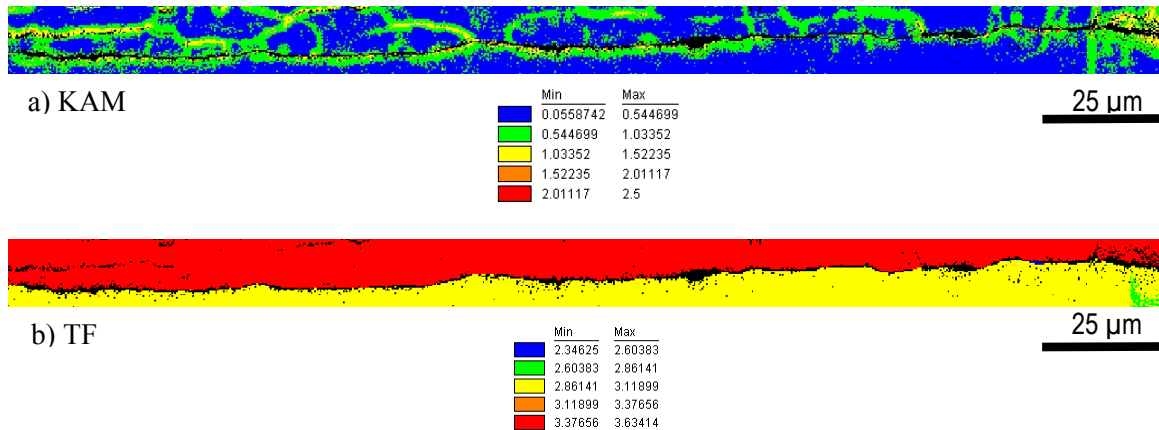


**Fig. 9    Correlation between KAM and TF for a typical delamination.    (a) KAM distribution along delamination and (b) TF distribution for grains bordering the delamination.**

## 5. Conclusions

Through this research, a repeatable and precise polishing method was developed, which is applicable to the study of many materials including Al-Li alloys. The refined mechanical polishing method was specifically tailored to generate high-quality EBSD and nanoindentation data in regions surrounding delamination without further surface preparation. Of interest in the study of Al-Li alloy 2090, emphasis was placed on several key microtexture analyses using EBSD such as: grain orientation and misorientation, kernel average misorientation (KAM), and Taylor factor (TF). Several interesting findings and correlations were drawn from the nano-scale and microstructural property variations near delamination fracture:

- Nanoindentation revealed small differences in hardness within the bulk of the sampled grains. However, KAM studies indicate that potentially higher variations in stored strain energy may exist along localized regions near delaminating grain boundaries.

- Brass grain orientations were found to be predominant in the mid-thickness region of the plate along with the presence of a dominant β-fiber. A tendency was observed for delaminations to be bordered by near-Σ3, twin-related brass variants.

- Boundaries susceptible to delamination were found to have significant differences in TFs between the adjacent grains.

- KAM revealed preferentially higher amounts of deformation along one side of delamination boundaries. These findings suggest that a lack of slip accommodation across interfaces may contribute to the increase in local deformation along one side.

- A correlation between KAM and TFs was observed: the grains with higher KAM were found to be low TF grains. The grains with significantly lower KAM corresponded to high TF grains. This correlation further supports our hypothesis for a lack of slip accommodations along boundaries which experience delamination.

16

**References**:

1.  Babel H, Gibson J, Tarkanian M et al (2007) 2099 Aluminum-Lithium with key-locked inserts for aerospace applications. J Mater Eng and Performance 16:584-591.
2.  Crooks R, Domack M, Wagner J (2005) Microtexture and nanoindentation study of delamination cracking in Al-Cu-Li-X alloys. Proceedings Materials Characterization,
3.  Oliver W, Pharr G (2004) Measurement of hardness and elastic modulus by instrumented indentation: Advances in understanding and refinements to methodology. J Mater Res 19:3-20.
4.  Elmustafa AA, Stone DS (2002) Indentation size effect in polycrystalline F.C.C. metals. Acta Mater 50:3641-3650.
5.  McNelley T, Swisher D, Pérez-Prado M (2002) Deformation bands and the formation of grain boundaries in a superplastic aluminum alloy. Metall and Mater Trans A 33:279-290.
6.  Bate PS, Huang Y, Humphreys FJ (2004) Development of the "brass" texture component during the hot deformation of Al-6Cu-0.4Zr. Acta Mater 52:4281-4289.
7.  Crooks R, Wang Z, Levit V et al (1998) Microtexture, microstructure and plastic anisotropy of AA2195. Mater Sci and Eng A257:145-152.
8.  Wagner J, Gangloff R (1992) Fracture toughness of an Al-Li-Cu-In alloy. Scr Metall 26:1779-1784.
9.  Kalyanam S, Beaudoin AJ, Dodds RH (2006) Characterization of the effect of delaminations – macrocrack and delamination driving forces. Project Sponsor Meeting: Huntsville, AL.
10. Takayama Y, Szpunar J (2004) Stored energy and Taylor factor relation in an Al-Mg-Mn alloy sheet worked by continuous cyclic bending. Mater Trans 45:2316-2325.